Characterizing seismic scattering in 3D heterogeneous Earth by a single parameter

Jagdish Chandra Vyas[1], Martin Galis[2,3] and Paul Martin Mai[1]

[1]*King Abdullah University of Science and Technology,*

[2]*Faculty of Mathematics, Physics and Informatics, Comenius University, Bratislava, Slovakia ,*

[3]*Earth Science Institute, Slovak Academy of Sciences, Bratislava, Slovakia*

Email: Jagdish.Vyas@kaust.edu.sa

Abstract

We derive a theoretical parameter for three seismic scattering regimes where seismic wavelengths are either much shorter, similar, or much longer than the correlation length of small-scale Earth heterogeneities. We focus our analysis on the power spectral density of the von Karman autocorrelation function, used to characterize the spatial heterogeneity of small-scale variations of elastic rock parameters that cause elastic seismic wave scattering. Our theoretical findings are verified by numerical simulations. We discover 1) that seismic scattering is proportional to the standard deviation of velocity variations in all three regimes, 2) that scattering is inversely proportional to the correlation length for the regime where seismic wavelengths are shorter than correlation length, but directly proportional to the correlation length in the other two regimes, and 3) that scattering effects are weak due to heterogeneities characterized by a gentle decay of the von Karman autocorrelation function for regimes where seismic wavelengths are similar or much longer than the correlation length.

Introduction

Heterogeneities in the Earth's crust and upper mantle cause seismic wave scattering, manifested in so-called seismic coda waves that trail the main seismic phases. Often, coda waves are prominent features of seismic recordings; they decay slowly with time, whereby the statistics of the temporal decay provide information about the scattering process and the medium through which the waves travelled (e.g. Aki 1969; Ritter et al., 1997; Sato and Fehler, 1998; Sato et al., 2012; Imperatori and Mai, 2013, 2015). After Aki's (1969) interpretation that coda waves are back-scattered energy from uniformly distributed heterogeneities in the Earth, several theoretical models were presented to explain seismic scattering, like the single scattering model, the multiple scattering model, the diffusion model, or the energy-flux model (Aki and Chouet, 1975; Sato, 1977; Gao et al., 1983; Frankel and Wennerberg, 1987). Additionally, the coda envelope broadens with increasing travel distance due to wavefield scattering (Sato 2016), a process that can be modelled employing a Markov approximation as stochastic treatment of the wave equation in random media (Sato et al., 2012; Sato 2016). In contrast, S-wave coda excitation is mainly dominated by scattering of direct S-waves from random heterogeneities in the Earth which can be modeled applying the Born approximation (Sato et al., 2012; Sato and Emoto, 2017). In summary, coda waves are seismic-wave energy trapped in the Earth due to the small-scale heterogeneities in the Earth.

Small-scale heterogeneities in the Earth can be described by a random spatial field superimposed onto a background homogeneous medium. For this purpose, several random-field models have been proposed; these are conveniently characterized by an autocorrelation function (ACF). For example, von Karman, Gaussian, exponential and Henyey–Greenstein ACF or a fractal distribution are used to describe random fields of seismic wave velocity variations in the Earth (e.g. Frankel and Clayton, 1986; Holliger and Levander, 1992; Sato and Fehler, 1998; Sato, 2019). Most commonly, the von Karman ACF is used (e.g.

Hartzell et al. 2010; Imperatori and Mai, 2013; Bydlon and Dunham, 2015). The power spectral density (PSD) of the von Karman AFC in three-dimension (3D) is given by

$$p(k_m) = \frac{\sigma^2 \, (2\sqrt{\pi}a)^3 \, \Gamma(H+1.5)}{\Gamma(H) \, (1 + k_m^2 a^2)^{(H+1.5)}}, \qquad (1)$$

where a, H, σ and Γ are correlation length, Hurst exponent, standard deviation and the Gamma function, respectively. We denote the wavenumber (2π/wavelength) of medium heterogeneity by k_m , and of the seismic wavefield by k_w, and write wavenumber k in case k_m and k_w can be used interchangeably.

Several studies examined the range for correlation lengths, standard deviation, and Hurst exponent in the Earth, both in observational studies and numerical simulations. Frankel and Clayton (1986) reported that velocity fluctuations with standard deviation of 5% and correlation lengths of 10 km (or greater) for 2D random media explain coda waves from micro earthquakes and travel time anomalies across seismic arrays. Holliger (1996) obtained correlation lengths of 10 to 100 meters and Hurst exponent in the range of 0.1 – 0.2 by analyzing sonic logs. Ritter et al. (1998) estimated wave-velocity perturbations of 3 – 7% and correlation length of 1 – 16 km for the lithosphere in central France. Recently, Sato (2019) reported that velocity perturbations are 1 – 10% in the Earth's crust and upper mantle and that the Hurst exponent typically falls in the range 0.0 – 0.5, while correlation lengths vary widely depending on sample size or dimension of the measurement system. Overall, standard deviation, Hurst exponent, and correlation lengths are found to be in the range of 1 – 10%, 0.0 – 0.5, and 1 – 15 km, respectively.

Seismic wave scattering occurs as the elastic waves encounter spatial variations of elastic medium properties. Whilst even the deterministic reflection of a seismic wave at an internal interface of a seismic velocity contrast could be classified as "seismic scattering", the common nomenclature is that seismic scattering is due to elastic-wave interactions with a spatially heterogeneous medium. In this context, the (statistical) characteristics of the scattered wavefield depend on the stochastic properties of the medium.

This concept is conveniently described considering the wavelengths (λ) or wavenumbers (k_w) of the elastic wave, and characteristic scales (wavelengths) of the random media.

Based on wavelength λ or wavenumber k_w of the seismic wave, and the correlation length a of the random media, seismic wave scattering can be classified into three regimes: (i) $k_w.a \gg 1$ ($\lambda \ll a$); (ii) $k_w.a \approx 1$ ($\lambda \approx a$); (iii) $k_w.a \ll 1$ ($\lambda \gg a$) (Sato and Fehler, 1998; Sato et al., 2012;). The regime $k_w.a \gg 1$ characterizes high-frequency scattering in which seismic wavelengths are much shorter than correlation lengths. This regime is important for the earthquake engineering community in the context of high-frequency (10 – 20 Hz) ground-shaking estimation, because seismic scattering redistributes seismic wave energy (i.e. ground-motion amplitudes) in space and time. The regime $k_w.a \approx 1$ represents the diffraction condition, the most fundamental type of scattering. Finally, the regime $k_w.a \ll 1$ denotes low-frequency scattering for which seismic wavelengths are much longer than the correlation length of the random medium. This regime is important for global seismology which uses primarily long wavelengths (0.01 – 0.5 Hz) to invert for the deterministic velocity structure of the Earth or earthquake source parameters (e.g. centroid moment tensors).

Numerical and theoretical studies investigating the effects of seismic scattering on earthquake ground-shaking suggest strong attenuation of ground-motion due to wavefield scattering (Shapiro and Kneib, 1993; Mai, 2009; Hartzell et al., 2010; Imperatori and Mai, 2012, 2013; Yoshimoto et al., 2015; Vyas et al., 2018). Bydlon and Dunham (2015) explained theoretically how the parameters describing the von Karman ACF control wavefield scattering in 2D. Using numerical simulations, they verified that a parameter $p_0 = \sigma/a^H$ determines the nature of scattering in the $k_w.a \gg 1$ limit, regardless of the specific values of σ and a. However, how the other parameters of the von Karman ACF (a, σ and H) affect 3D seismic scattering has not been explored yet in detail.

Here, we investigate seismic wave scattering in 3D and verify our theoretical results by numerical simulations. First, we examine the mathematical expression for the power spectral density (PSD) of the von Karman AFC (Eq. 1) to identify parameters that represent scattering behaviour in 3D for the three different regimes, $k_w.a \gg 1$, $k_w.a \approx 1$ and $k_w.a \ll 1$. Then we test our theoretical findings through numerical simulations that cover the parameter space of these three regimes and allow us to examine how scattering manifests itself in seismic waveforms and ground-motion amplitudes.

Theory

Bydlon and Dunham (2015) investigated high-frequency scattering (f = 1 – 30 Hz) by considering a 2D problem and the regime $k_w.a \gg 1$. To analyze scattering under these assumptions, they simplified the PSD of the von Karman ACF to obtain the root-mean-square (RMS) fluctuations of normalized seismic wave velocity (wave speed), and then derived which parameters (i.e., a, H and/or σ) control wavefield scattering. Here, we extend their approach to 3D by considering three different $k_w.a$ regimes.

Wavefield scattering is strongest if the wavenumber of the seismic wave is comparable to the wavenumber of heterogeneities in the medium. Hence, we simplify the PSD for the three regimes ($k_w.a \gg 1$, $k_w.a \approx 1$ and $k_w.a \ll 1$) under the diffraction condition to obtain RMS of fluctuations of normalized wave velocity (computed as the square root of the mean power, denoted as P_{RM}). By assuming the diffraction condition, we derive theoretically the parameter P_{RM}, which in fact dictates the wavefield scattering in 3D. Seismic scattering associated with a particular seismic wavelength will depend on the amplitudes of velocity variations corresponding to that wavelength. However, we aim to understand the overall wavefield scattering behaviour for a range of seismic wavelengths and heterogeneity scales in the medium. Therefore, our P_{RM} derivations are not only applicable for a monochromatic source or a single-wavelength medium, but instead capture the broadband nature of scattering. Note that we only summarize the final equations for P_{RM} for each regime in the main text; further details of the derivations are provide in the Electronic supplement.

Regime I: $k_w.a \gg 1$

Our P_{RM} derivation for this regime assumes that the source excites waves of equal amplitude (a flat source spectrum) with wavenumbers from k_{min} to infinity, all of which interact with heterogeneities in the medium with the same range of wavenumbers (albeit at different "intensity" or strength). Note that this assumption is not completely satisfied in nature as earthquakes typically excite only a limited range of frequencies, and not all of these frequencies will interact with the generally scale-limited medium heterogeneities. However, the assumption allows us to calculate the overall wavefield scattering behaviour for the regime $k_w.a \gg 1$, for which seismic wavelengths are much shorter than the correlation length of small-scale Earth heterogeneities. Then, the RMS fluctuations of normalized wave velocity (P_{RM}) can be approximated by

$$P_{RM} = \sqrt{\frac{1}{4\pi}\int_{k_{min}}^{\infty} p(k)\, k^2\, dk} \approx \sqrt{(c_0 + c_1\, H + c_2\, H^2)}\;\; \frac{\sigma}{a^H}\, \frac{\pi^{1/4}}{k_{min}^H} \qquad (2)$$

Therefore, the P_{RM} dependency is given by,

$$P_{RM} \propto \sqrt{(c_0 + c_1\, H + c_2\, H^2)}\;\; \frac{\sigma}{a^H}\,, \qquad (3)$$

where we approximate the term depending on H by a quadratic function (with coefficients c_0= 0.89, c_1= 0.53, and c_2= -0.08; see Fig. S1a and derivation in electronic supplement for details). Note that we characterize the scattering behavior for the entire regime $k_w.a \gg 1$, rather than for a particular wavelength in this regime by using integration limits in Eq. 2 from k_{min} to infinity, and not over any arbitrary wavenumber range. Therefore, the parameter P_{RM} (Eq. 3) becomes independent of wavenumber.

Comparing Eq. 3 with parameter $p_0 = \sigma/a^H$ (Bydlon and Dunham, 2015) reveals that even in the regime $k_w.a \gg 1$, scattering in 3D is more complex than in 2D. Eq. 3 illustrates that in the high-frequency scattering regime, (a) scattering is proportional to the standard deviation of the velocity fluctuations, (b) scattering is inversely proportional to the correlation length a, and c) the Hurst exponent has a strongly non-linear effect on scattering. Interestingly, if the Hurst exponent approaches its theoretical lower limit of zero (H→0), Eq. 3 can be further simplified to

$$P_{RM} \;\propto\; \sigma\,, \qquad (4)$$

indicating that scattering is controlled by the standard deviation of the velocity variations in this case.

Regime II: $k_w.a \approx 1$

We assume that the source excites waves having a flat source spectrum with wavenumbers from k_1 to k_2, all of which interact with medium heterogeneities of the same wavenumber range. If seismic wavelengths are comparable to the correlation length of heterogeneities, the RMS fluctuations of normalized wave velocity can be approximated by

$$P_{RM} \;=\; \sqrt{\frac{1}{4\pi}\int_{k_1}^{k_2} p(k)\,k^2\,dk} \;\approx\; \left(\frac{\pi}{18}\right)^{1/4} a^{3/2}\sigma\,\sqrt{(c_1\,H + c_2\,H^2)}\,\sqrt{(k_2^3 - k_1^3)} \quad (5)$$

Therefore, the P_{RM} dependency is given by,

$$P_{RM} \;\propto\; \sqrt{(c_1\,H + c_2\,H^2)}\,a^{3/2}\sigma, \qquad (6)$$

Where coefficients are given as c_1= 0.93, and c_2= -0.27 (see Fig. S1b). Analyzing Eq.6 for P_{RM} reveals that a) scattering is proportional to σ, similar to the regime $k_w.a \gg 1$, b) scattering is proportional to correlation length a, in contrast to regime $k_w.a \gg 1$ (compare Eq. 6 with Eq. 3), and c) scattering is correlated with the Hurst exponent (as H approaches zero, scattering effects weaken and become eventually negligible).

Regime III: $k_w.a \ll 1$

Here, we assume that the source excites waves of equal amplitude (a flat source spectrum) with wavenumbers from zero to k_1, all of which interact with medium heterogeneities. If seismic wavelengths are much longer than the correlation length of the heterogeneities, the RMS fluctuations of normalized wave velocity can be approximated by

$$P_{RM} = \sqrt{\frac{1}{4\pi}\int_0^{k_1} p(k)\, k^2\, dk} \approx \left(\frac{4\pi}{9}\right)^{1/4} a^{3/2}\sigma \sqrt{(c_1\, H + c_2\, H^2)}\, k_1^{3/2} \qquad (7)$$

Therefore, the P_{RM} dependency is given by

$$P_{RM} \propto \sqrt{(c_1\, H + c_2\, H^2)}\, a^{3/2}\sigma, \qquad (8)$$

where coefficients c_1= 0.93, and c_2= 0.40 (see Fig. S1c). Note that only constant c_2 is different between Eq. 8 and Eq. 6, therefore, P_{RM} for the regime $k_w.a \ll 1$ is similar to that for $k_w.a \approx 1$, except that the effect of H on scattering is stronger for $k_w.a \ll 1$ than for $k_w.a \approx 1$ because $c_2 > 0$ (compare Eq. 6 and Eq. 8).

Verification of Theory by Simulations

In this section, we verify our findings (Eq. 3, 4, 6, 8) by conducting seismic wavefield simulations in random media. Since our simulations do not strictly satisfy the assumptions used for the derivations of P_{RM}, we validate only proportionality or inverse-proportionality of P_{RM} with correlation length, standard deviation, and Hurst exponent, rather than the complete expressions (Eq. 3, 4, 6, 8). To numerically test our results for the three scattering regimes, we fix the correlation length a and modify the source frequency to radiate seismic waves with different frequencies (i.e., we are altering the wavenumber k_w). For computing synthetic seismograms, we use a generalized 3D finite-difference method with secondorder accuracy in space and time (SORD code by Ely et al., 2008). Our simulations consider several discretized Earth models, a point-source earthquake model, and receiver locations at which ground-motions are stored. We then analyze waveforms and peak ground acceleration (PGA), and confront the numerical results with our theoretical analysis.

Set up for Numerical Modeling

We consider a point source (moment magnitude M_W ~2.84) at a depth of 7.5 km, with strike, dip, and rake of 22.5°, 90°, and 0°, respectively. The source-time function (STF) is a Gaussian. We define STFs to radiate frequencies required to properly sample the three regimes (f_{max} = 5.0 Hz for $k_w.a \gg 1$, f_{max} = 0.5 Hz for $k_w.a \approx 1$ and f_{max} = 0.03 Hz for $k_w.a \ll 1$, see Fig S2; f_{max} is the high frequency limit of the flat portion of the slip velocity spectrum). For example, a point source radiating frequencies of 5.0 Hz, 0.5 Hz and 0.03 Hz in a heterogeneous medium with background shear-wave velocity 3.464 km/s and stochastic perturbations with correlation length of 1 km yields $k_w.a \approx$ 9.0, 0.9 and 0.05, respectively.

To create a velocity model with small-scale heterogeneities, we add random-field variations of seismic wave velocities, characterized by an isotropic von Karman ACF, to the uniform background Earth model (with S-wave velocity 3464 m/s, P-wave velocity, 6000 m/s, and density 2700 kg/m^3). In total, we generate twelve 3D computational models (M1 to M12; Table 1), considering three correlation lengths (1.0 km, 5.0 km, 10.0 km), two values of standard deviation (5%, 10%), and two Hurst exponents (0.1, 0.5). For each combination of medium parameters, we create one realization of random inhomogeneity in S-wave speed, P-wave speed, and density. S-wave velocity distributions at the surface are shown for all twelve computational models (Figs 1a, 1b). Theoretical 1D power spectra for seven selected models are plotted to illustrate effects of correlation lengths, standard deviation, and Hurst exponent on the spectral shape (Fig 1c). Power spectra for two specific models, M2 and M11, are examined for the three scattering regimes considering the three STFs used in this study (Fig. 1d).

The size of the computational domain must be chosen such that seismic waves propagate to large-enough distances that ensure sufficient wave interaction with medium heterogeneities to develop scattering. At the same time, the domain should be as small as possible to minimize computational cost. Given these constraints, we define different computational domain sizes and grid spacings, depending on scattering regime. For the regime $k_w.a \gg 1$, we use grid spacing h=25m (dt=0.0015 s) on a domain of 60x60x15 km, allowing travel distance of ~40 wavelengths (at f = 5.0 Hz). Combining these models with STF1 (Fig. S2a) yields $k_w.a$ in the range of 9 to 90. For $k_w.a \approx 1$ we use h=75m (dt=0.0045 s) and a larger domain, 355x355x30 km, corresponding to travel distance of ~50 wavelengths (at f = 0.5 Hz). The eight corresponding models are denoted by the suffix "-L" (see Tab 1 and Fig S3) and when combined with STF2 (Fig. S2b), they result in $k_w.a$ -values between 0.9 and 4.5. For $k_w.a \ll 1$, we use h=1000m (dt=0.055 s) and an extra-large domain, 2000x2000x60 km (ignoring the spherical nature of Earth), denoted by the suffix "-EL" (see Tab 1 and Fig S4). When combined with STF3 (Fig. S2c), the corresponding $k_w.a$ values fall in the range 0.27 to 0.5. Owing to the very long wavelengths in this regime (~115km at f = 0.03 Hz), the domain allows travel distances of only ~15 wavelengths, significantly lower than those in the two previous regimes. However, the cost for computational models allowing travel distances of ~45-50 wavelengths would be exorbitant. In total, we use 28 computational models with random inhomogeneities, twelve of which are for $k_w.a \gg 1$, eight for $k_w.a \approx 1$ and eight for $k_w.a \ll 1$ regimes. Our simulations consumed nearly four million core-hours of computational resources on a Cray XC40 supercomputer. To establish a base case for comparison, we also conduct simulations in a homogeneous medium for each regime.

We store synthetic seismograms at receivers placed in a concentric rings for $k_w.a \gg 1$, but for $k_w.a \approx 1$ and $k_w.a \ll 1$ we consider only a one quadrant to save computational costs (Fig 1a, Fig S3a, Fig S4a). The epicenter is placed in the center of the simulation domain for $k_w.a \gg 1$, but for $k_w.a \approx 1$ and $k_w.a \ll 1$

it is in the lower left corner. Receiver geometry and epicenter location are designed to obtain the best possible azimuthal coverage of stations and to allow for sufficiently large travel distances for seismic waves to develop scattering, at the same time also minimizing computational costs. Virtual stations are distributed along rings with radial spacing of 0.1, 0.2 and 3.5 km, for $k_w.a \gg 1$, $k_w.a \approx 1$ and $k_w.a \ll 1$ regimes, respectively. Therefore, each ring (arc) of stations contains a different number of stations at different azimuths. The smallest ring (arc) used for PGA statistics has 314 (radius 5km), 196 (radius 25 km) and 134 (radius 300 km) stations for the three regimes ($k_w.a \gg 1$; $k_w.a \approx 1$; $k_w.a \ll 1$). Therefore, our receiver geometry is statistically independent and PGA statistics are robust. All waveforms are low-pass filtered using a fourth-order Butterworth filter with cutoff frequencies of 5 Hz, 0.5 Hz and 0.03 Hz for the three scattering regimes, respectively.

Quantifying Seismic Scattering in Numerical Results

Seismic scattering redistributes energy in space and time from direct P- and S-waves into the late-arriving coda waves. Consequently, peak ground acceleration (PGA) in a homogeneous medium will be, on average, higher than in a scattering medium. Therefore, we examine ratios of PGA-values to quantify scattering "strength" in numerical simulations. Horizontal components of acceleration are mostly used in earthquake engineering applications (e.g., Boore and Atkinson, 2008; Chiou and Youngs, 2008), because wave amplitudes on the vertical component are usually smaller than on the horizontal components. Therefore, we analyze horizontal PGA (computed as maximum magnitude of acceleration from the two horizontal components). We illustrate scattering effects and resulting PGA values by comparing waveforms for selected receivers s1, s2 and s3 (see Fig 1a for their locations).

In Fig 2 we compare horizontal-component ground-acceleration waveforms at selected stations for the regime $k_w.a \gg 1$. Fig 2a compares waveforms and PGA values for two values of standard deviation (models M3 and M6) with those for the homogeneous medium PGA values are consistent with our expectation that stronger scattering leads to lower PGA. In this particular case, the scattering for model M3 is weaker than for model M6 (see also acceleration snapshots in Fig S5). Additionally, ground acceleration comparison for M6 at three stations (Fig S6) shows prominent coda evolution and reduced maximum acceleration values as epicentral distance increases (from s4 to s6). Fig 2b reveals that waveforms for two models with different correlation lengths (M1 and M3) are almost identical, with only small time shifts. This indicates that the two models yield almost identical levels of scattering (confirmed also by comparing acceleration snapshots for M1 and M3 in Fig S5). Correspondingly, PGA values are comparable. In addition, these comparisons (Figs 2a and 2b) suggest that scattering is primarily controlled by the standard deviation of the medium heterogeneities, whereas the correlation length has a negligible effect for a small H value ($H = 0.1$), consistent with our theoretical analysis in Eq. 4. However, we note that PGA only works well in such comparisons because we computed a reference solution for the homogeneous medium. Without such a reference case, interpreting PGA values directly as indicator for "scattering strength" would be misleading.

Statistical Analysis of Scattering

Next, we calculate the mean and standard deviation of PGA values for all stations at a given epicentral distance and for a given computational model (see Fig. S7 for a comparative summary of all computational models). To estimate the average scattering-related PGA reduction at a given epicentral distance, we define the "mean PGA ratio" (MPR), at a particular epicentral distance, as the ratio between the mean PGA values from any heterogeneous Earth model to the mean PGA-values from the reference homogeneous Earth model. As epicentral distance increases, the MPR is expected to decrease because the redistribution of seismic energy due to scattering is cumulative with propagation distance.

Figure 3 summarizes our results for $k_w.a \gg 1$. For H = 0.1 we find the MPRs for models with σ = 10% (M4, M5, M6) are lower than for models with σ 5% (M1, M2, M3) (Fig. 3a). At the same time, MPRs of both groups are very similar, supporting our theoretical conclusion that for small H the correlation length has insignificant effects on scattering, which in this regime is controlled by standard deviation (Eq. 4). The apparent plateau in MPRs for distances 10 to 20 km is a consequence of source effects being masked by wavefield scattering effects due to the hypocenter location (see Fig. S8 for more details on the effects of hypocentral depths on MPRs). Fig 3b compares solutions for H=0.5, for which we expect a significant effect of both correlation length and standard deviation. For fixed σ, we observe that the MPR's for models with shorter correlation length are lower than those with longer correlation length (MPR_{M7} < MPR_{M8} < MPR_{M9}; similarly MPR_{M10} < MPR_{M11} < MPR_{M12}). This finding is consistent with our conclusion that scattering is inversely proportional to correlation length for large H (Eq. 3). Also, MPR's for models with σ = 10% are lower than those for corresponding models with σ = 5% (MPR_{M10} < MPR_{M7}, MPR_{M11} < MPR_{M8}, MPR_{M12} < MPR_{M9}), demonstrating that scattering is proportional to the standard deviation of velocity variations for large H. Thus, these observations validate our theoretical conclusions for the regime $k_w.a \gg 1$.

The MPR-analysis for regime $k_w.a \approx 1$ is summarized in Figure 4. For both values of H, the MPR's for models with shorter correlation length are higher than MPR's for models with longer correlation length (MPR_{M1-L} > MPR_{M2-L}, MPR_{M4-L} > MPR_{M5-L}, MPR_{M7-L} > MPR_{M8-L}, MPR_{M10-L} > MPR_{M11-L}), revealing that scattering is proportional to correlation length (see Fig. 4a and Fig. 4b). The MPR's for models with σ = 5% are higher than those for model with σ = 10% (MPR_{M1-L} > MPR_{M4-L}, MPR_{M2-L} > MPR_{M5-L}, MPR_{M7-L} > MPR_{M10-L}, MPR_{M8-L} > MPR_{M11-L}), indicating that scattering is proportional to the standard deviation of velocity fluctuations. The MPR's for models with H = 0.1 are larger than those for models with H = 0.5 (MPR_{M1-L} > MPR_{M7-L}, MPR_{M2-L} > MPR_{M8-L}, MPR_{M4-L} > MPR_{M10-L},

MPR_{M5-L} > MPR_{M11-L}), therefore, scattering is proportional to the Hurst exponent *H*. These observations are also consistent with our theoretical findings for $k_w.a \approx 1$ (see Eq. 6).

Finally, we show MPR statistics for the regime $k_w.a \ll 1$ (Figure 5). First, recall that due to prohibitively large computational costs we used a smaller computational domain (see Section *Set up for Numerical Modeling*). Consequently, scattering is less well developed for $k_w.a \ll 1$, and hence effects on MPR's are not as pronounced as in the other two regimes. Still, the effects are strong enough to support our theoretical derivation (see waveform comparison in Fig. S9 and station locations in Fig. S4). The MPR's for models with 10 km correlation length are lower than those for 5 km correlation length (MPR_{M3-EL} < MPR_{M2-EL}, MPR_{M6-EL} < MPR_{M5-EL}, MPR_{M9-EL} < MPR_{M8-EL}, MPR_{M12-EL} < MPR_{M11-EL}), showing that scattering is proportional to correlation length. The MPR's for models with σ = 10% are lower than those for σ = 5% (MPR_{M12-EL} < MPR_{M9-EL}, MPR_{M11-EL} < MPR_{M8-EL}), suggesting that scattering is also proportional to the standard deviation of velocity variations. These observations agree well with our theoretical considerations for $k_w.a \ll 1$ (see Eq. 8).

In summary, our results from numerical simulations are consistent with our conclusions based on theoretical derivation for all three considered scattering regimes.

Discussion and Conclusions

We derive a new parameter P_{RM} to quantify 3D seismic wavefield scattering. P_{RM} is based on the assumption that small-scale heterogeneities in seismic velocity are characterized by the von Karman ACF. P_{RM} helps to understand the influence of the parameters of the von Karman ACF on seismic scattering for three considered regimes ($k_w.a \gg 1$, $k_w.a \approx 1$ and $k_w.a \ll 1$). We test our theoretical consideration through statistical analysis of a suite of numerical simulations that capture seismic scattering in different scattering regimes.

We find that the strength of wavefield scattering in all three regimes is proportional to the standard deviation of heterogeneities. Seismic scattering is also proportional to the correlation length in the regimes $k_w.a \approx 1$ and $k_w.a \ll 1$, but for the regime $k_w.a \gg 1$ the scattering is inversely proportional to correlation length. For regime $k_w.a \gg 1$, we also find that if the Hurst exponent H approaches zero, scattering will be controlled solely by standard deviation. However, for $k_w.a \approx 1$ and $k_w.a \ll 1$, scattering is weakly impacted for small values of H, with scattering vanishing in the limit of H →0.

To further explain these findings, we integrate the PSD for the 3D problem (Eq. 1) with respect to wavenumber k_m,

$$\int_0^\infty p(k_m)\, dk_m = 4\pi^2 a^2 \sigma^2 H \qquad (9)$$

Eq. 9 represents the area under the power spectrum for a three dimensional isotropic PSD along one wavenumber axis; it reveals that the area under the power spectrum depends on a, H and σ, implying also that the area under the power spectrum will be zero if any of a or H or σ is zero. For example, M2 has larger area under the power spectrum than M1 due to larger correlation lengths of M2, although standard deviation and Hurst exponent are identical for M1 and M2 (see Fig. 1c). The area under the power spectrum can be linked to wavefield scattering as it represents the total scattering power of the heterogeneous medium in terms of the sum of amplitude squares of seismic-velocities. Correspondingly, in the limit of any of the von Karman parameters approaching zero, wavefield scattering will become negligible.

Quantitative analysis of power spectra in Fig 1c helps to interpret the implications of Eq. 9 for the three scattering regimes. Therefore, our theoretical findings, confirmed by numerical simulations, can be explained by the amplitude and shape of the PSD. The standard deviation scales the power spectra without changing the shape of the power spectra (hence, area under the power spectra), resulting in scattering proportional to σ for all three regimes ($k_w.a \gg 1$, $k_w.a \approx 1$ and $k_w.a \ll 1$). The tails of the power spectra (decaying part) show inverse proportionality with correlation length a (e.g. compare tails of M7, M8 and M9 in Fig 1c), thus resulting in scattering being inversely proportional to a for the regime $k_w.a \gg 1$. However, the plateau and corners (corner wavenumber = $2\pi/a$) of the power spectra scale with correlation length, leading to scattering being proportional to correlation length for $k_w.a \ll 1$ and $k_w.a \approx 1$, respectively (e.g. compare plateau and corners of M7, M8 and M9 in Fig 1c). Furthermore, the plateau and corner of power spectra grow as H increases, therefore, scattering is proportional to H for $k_w.a \ll 1$ and $k_w.a \approx 1$. Fig 1c also shows that the tails of the power spectra tend to merge for small H (see M1, M2 and M3) and diverge as H increases (compare M7, M8 and M9), implying a more complex dependency on H for scattering in the regime $k_w.a \gg 1$. Hence, our findings can be explained by the shape and amplitude of the PSD function of the von Karman ACF.

Comparing our results for $k_w.a \gg 1$ for the 3D problem (Eq. 3) with the 2D results by Bydlon and Dunham (2015) ($p_0 = \sigma/a^H$) reveals that the effect of standard deviation and correlation length remains the same, but the effect of the Hurst exponent H is stronger in 3D. However, if the Hurst exponent approaches zero, scattering effects are dominated by standard deviation, both in 2D and 3D. This is an important finding, since values of H smaller than 0.5 have been reported by Sato (2019) for the Earth's crust and mantle.

Here we propose to quantify the overall wavefield scattering directly via an integral of the PSD function of the random media. We note that Sato et al. (2012) analyzed a plane wave scattered by a localized inhomogeneity using the wave equation. They solved the wave equation utilizing Born approximation, i.e., they assumed that the amplitude of velocity variations is negligibly small compared to background velocity, that the amplitude of the scattered wavefield is negligibly small compared to the amplitude of incident wavefield, and that the scattered wavefield has only a small phase change after passing through the heterogeneity. Therefore, derivations by Sato et al., (2012) are valid for high frequency scattering, when seismic wavelengths are very short compared to the length scales of medium heterogeneity. They found that the scattering coefficient depends on the PSD function of the random media as follows (Eq. 4.25 from Sato et al., 2012),

$$g(\theta, \omega) = \frac{k_w^4}{\pi} P(2k_w \, sin\frac{\theta}{2}) \qquad (10)$$

In Eq. 10, θ is the angle between incident and scattered waves; ω and k_w are angular frequency and wavenumber of the incident wavefield, respectively. The scattering coefficient reveals that a wave with wavenumber k_w interacts with medium heterogeneities with wavenumber k_m, leading to

$$k_m = 2k_w \, sin\frac{\theta}{2} = 2 \, sin\frac{\theta}{2} \, k_w = C \, k_w \qquad (11)$$

The scaling factor C is a function of the scattering angle θ and ranges from 0 to 2, for forward (θ = 0) and backward (θ = π) scattering, respectively. The average value of C (over θ) indicates the overall interaction between k_m and k_w, averaged over all directions. The average value of C is 1.27, therefore $k_m \sim k_w$. This is consistent with our assumption for the derivation of P_{RM} , although we apply an ideal diffraction condition ($k_m = k_w$). Note that our P_{RM} results will not change even if we use a more relaxed diffraction condition (i.e. $k_m \sim k_w$). Hence, our theory complies with Sato et al. (2012), but taking a different perspective on evaluating the wavefield scattering. Note that the detailed theoretical analysis to fully describe the wavefield scattering in 3D requires considering the 3D elastic wave equation with complex earthquake source characteristics (radiated wavefield) in 3D random media with anisotropic wave propagation. This derivation is beyond the scope of the present study.

In summary, our theoretical analysis of the von Karman PSD, used to represent random spatial variation in seismic wave velocities and rock density, helps to develop a physics-based understanding of how standard deviation, correlation length, and Hurst exponent govern three-dimensional seismic wavefield scattering for three scattering regimes ($k_w.a \gg 1$, $k_w.a \approx 1$ and $k_w.a \ll 1$). This will help studies on ground-motion simulations for earthquake shaking as well as research on global seismic wave propagation in 3D Earth models to properly simulate elastic wavefield scattering.

Data and Resources

Ground-motions simulations carried out to verify the outcomes of theoretical derivation generated nearly 2.5 TB of data which can be provided via personal communication. This manuscript has an electronic supplement which comprises the complete derivation of the root-mean-square fluctuations of normalized wave velocity using power spectral density of the von Karman autocorrelation function for three scattering regimes ($k_w.a \gg 1$, $k_w.a \approx 1$ and $k_w.a \ll 1$). The electronic supplement also contains figures of the quadratic fit to ratios of gamma functions, three Gaussian source time functions, simulations setup depicting receiver geometry and S-wave speed variations, acceleration waveforms comparison from few receivers, snapshots of ground-acceleration wavefield at Earth surface and peak ground acceleration statistics.

Acknowledgements

The research presented in this article is supported by King Abdullah University of Science and Technology (KAUST) in Thuwal, Saudi Arabia, grants BAS/1/1339-01-01 and URF/1/3389-01-01. MG was partially supported by Scientific Grant Agency VEGA, grant 2/0046/20. Earthquake ground-motion simulations have been carried out using the KAUST Supercomputing Laboratory (KSL), and we acknowledge the support of the KSL staff. We thank Art Frankel and an anonymous reviewer, as well as the editor Adrien Oth, for their constructive critical review that helped us to improve the manuscript.

References

Aki, K. (1969). Analysis of the seismic coda of local earthquakes as scattered waves. Journal of geophysical research, 74(2), 615-631.

Aki, K., & Chouet, B. (1975). Origin of coda waves: source, attenuation, and scattering effects. Journal of geophysical research, 80(23), 3322-3342.

Boore, D. M., & Atkinson, G. M. (2008). Ground-motion prediction equations for the average horizontal component of PGA, PGV, and 5%-damped PSA at spectral periods between 0.01 s and 10.0 s. Earthquake Spectra, 24(1), 99-138.

Bydlon, S. A., & Dunham, E. M. (2015). Rupture dynamics and ground motions from earthquakes in 2-D heterogeneous media. Geophysical Research Letters, 42(6), 1701-1709.

Chiou, B. J., & Youngs, R. R. (2008). An NGA model for the average horizontal component of peak ground motion and response spectra. Earthquake Spectra, 24(1), 173-215.

Ely, G. P., Day, S. M., & Minster, J. B. (2008). A support-operator method for viscoelastic wave modelling in 3-D heterogeneous media. Geophysical Journal International, 172(1), 331-344.

Frankel, A., & Clayton, R. W. (1986). Finite difference simulations of seismic scattering: Implications for the propagation of short-period seismic waves in the crust and models of crustal heterogeneity. Journal of Geophysical Research: Solid Earth, 91(B6), 6465-6489.

Frankel, A., & Wennerberg, L. (1987). Energy-flux model of seismic coda: separation of scattering and intrinsic attenuation. Bulletin of the Seismological Society of America, 77(4), 1223-1251.

Gao, L. S., Biswas, N. N., Lee, L. C., & Aki, K. (1983). Effects of multiple scattering on coda waves in three-dimensional medium. pure and applied geophysics, 121(1), 3-15.

Hartzell, S., Harmsen, S., & Frankel, A. (2010). Effects of 3D random correlated velocity perturbations on predicted ground motions. Bulletin of the Seismological Society of America, 100(4), 1415-1426.

Holliger, K. (1996). Upper-crustal seismic velocity heterogeneity as derived from a variety of P-wave sonic logs. Geophysical Journal International, 125(3), 813-829.

Holliger, K., & Levander, A. R. (1992). A stochastic view of lower crustal fabric based on evidence from the Ivrea zone. Geophysical Research Letters, 19(11), 1153-1156.

Imperatori, W., & Mai, P. M. (2012). Sensitivity of broad-band ground-motion simulations to earthquake source and Earth structure variations: an application to the Messina Straits (Italy). Geophysical Journal International, 188(3), 1103-1116.

Imperatori, W., & Mai, P. M. (2013). Broad-band near-field ground motion simulations in 3-dimensional scattering media. Geophysical journal international, 192(2), 725-744.

Imperatori, W., & Mai, P. M. (2015). The role of topography and lateral velocity heterogeneities on near-source scattering and ground-motion variability. Geophysical Journal International, 202(3), 2163-2181.

Mai, P. M. (2009). Ground Motion: Complexity and Scaling in the Near Field of Earthquake Ruptures. Encyclopedia of Complexity and System Sciences, R. Meyers (Editor), Springer, ISBN 978-0-387-69572-3,pp 4435–4474.

Ritter, J. R., Mai, P. M., Stoll, G., & Fuchs, K. (1997). Scattering of teleseismic waves in the lower crust observations in the Massif Central, France. Physics of the earth and planetary interiors, 104(1-3), 127-146.

Ritter, J. R., Shapiro, S. A., & Schechinger, B. (1998). Scattering parameters of the lithosphere below the Massif Central, France, from teleseismic wavefield records. Geophysical Journal International, 134(1), 187-198.

Sato H., & Fehler, M. C. (1998). Seismic Wave Propagation and Scattering in the Heterogenous Earth, , Springer-Verlag, New York, ISBN #0-387-98329-5.

Sato, H. (1977). Single isotropic scattering model including wave conversions simple theoretical model of the short period body wave propagation. Journal of Physics of the Earth, 25(2), 163-176.

Sato, H. (2016). Envelope broadening and scattering attenuation of a scalar wavelet in random media having power-law spectra. Geophysical Journal International, 204(1), 386-398.

Sato, H. (2019). Power spectra of random heterogeneities in the solid earth. Solid Earth, 10(1), 275-292.

Sato, H., & Emoto, K. (2017). Synthesis of a scalar wavelet intensity propagating through von Kármán-type random media: joint use of the radiative transfer equation with the Born approximation and the Markov approximation. Geophysical Journal International, 211(1), 512-527.

Sato, H., Fehler, M. C., & Maeda, T. (2012). Seismic wave propagation and scattering in the heterogeneous earth. Springer Science & Business Media. ISBN 978-3-642-23028-8.

Shapiro, S. A., & Kneib, G. (1993). Seismic attenuation by scattering: theory and numerical results. Geophysical Journal International, 114(2), 373-391.

Vyas, J. C., Mai, P. M., Galis, M., Dunham, E. M., & Imperatori, W. (2018). Mach wave properties in the presence of source and medium heterogeneity. Geophysical Journal International, 214(3), 2035-2052.Yoshimoto, K., Takemura, S., & Kobayashi, M. (2015). Application of scattering theory to P-wave amplitude fluctuations in the crust. Earth, Planets and Space, 67(1), 199.

Author's full physical mailing addresses:

Dr. Jagdish Chandra Vyas,
Building 1, Level 3, office #3110,
King Abdullah University of Science and Technology (KAUST),
Jeddah, Thuwal, 23955, Saudi Arabia.

Dr. Martin Galis,
Department of Astronomy, Physics of the Earth, and Meteorology,
Faculty of Mathematics, Physics and Informatics,
Comenius University,
Mlynska dolina F1,
842 48 Bratislava,
Slovakia.

Prof. Paul Martin Mai,
Building 1, Level 3, office #3114,
King Abdullah University of Science and Technology (KAUST),
Jeddah, Thuwal, 23955, Saudi Arabia.

List of Table Captions

Table 1: Parameters for the 28 computational 3D Earth models generated for this study.

List of Figure Captions

Figure 1: (a,b): S-wave speed distribution at the free surface for twelve 3D computational models for the regime $k_w.a \gg 1$, generated using three correlation lengths (1.0 km, 5.0 km, 10.0 km), two standard deviations (5%, 10%) and two Hurst exponents (0.1, 0.5). The black star marks the epicenter. The sites used for waveform comparison (black triangles, s1, s2, s3, s4, s5 and s6) and ground-motion analysis (black dots in circular rings) are also shown. The beach ball shows the focal mechanism of the earthquake source. Panels (a) and (b) depict random media with Hurst exponent 0.1 and 0.5, respectively. **(c):** Theoretical 1-D power spectra (PSD) for 3D Earth structure for seven selected models. Correlation length and Hurst exponent alter the shape of the power spectra (solid lines), whereas standard deviation only scales the PSD (mark dashed line; notice the scaling of M4 compared to M1, but their identical shape). **(d):** The theoretical power spectra of the random media are constrained by the dimensions of the computational model and the spatial grid size. The dashed and solid lines are spectra related to models M2 and M11, whereas three different colors depict power spectra sampled according to the three scattering regimes.

Figure 2: Horizontal components (East-West, EW, and North-South, NS) of ground acceleration (m/s^2) at sites s1, s2, s3 (Fig 1a). Black dotted lines indicate theoretical P- and S-wave arrival times in the considered homogeneous medium. Color-coded numbers indicate PGA values at individual sites. Waveforms are normalized by their PGA-value in the homogeneous-medium simulations for a given site. (a) Illustration

of scattering controlled by σ for $k_w.a \gg 1$ and small H; (b) Illustration of negligible effects of correlation length on scattering for $k_w.a \gg 1$ and small H.

Figure 3: Mean PGA ratios (MPR) for all twelve numerical simulations as a function of distance, depicting the effects of wavefield scattering on ground-motions in the regime $k_w.a \gg 1$. Panels (a) and (b) depict MPR for media with H=0.1 and H=0.5, respectively. Grey dashed lines are plotted to facilitate the MPR comparison in two nearby panels. Wavefield scattering is proportional to the standard deviation of medium heterogeneities, and inversely proportional to correlation length for large Hurst exponent (H= 0.5), but remains nearly unaffected by variations in correlation length for small Hurst exponent (H= 0.1). The $k_w.a$ maxima for correlation lengths of 1, 5 and 10 km are 9.07, 45.36 and 90.72, respectively.

Figure 4: Mean PGA ratios (MPR) for eight numerical simulations as a function of distance, depicting the effects of wavefield scattering on ground-motions in the regime $k_w.a \approx 1$. Panels (a) and (b) depict MPR for media with H=0.1 and H=0.5, respectively. Grey dashed lines are plotted to facilitate the MPR comparison in two nearby panels. Wavefield scattering is proportional to correlation length, Hurst exponent, and standard deviation of medium heterogeneities. The highest values of $k_w.a$ for correlation lengths of 1 and 5 km are 0.90 and 4.53, respectively.

Figure 5: Mean PGA ratios (MPR) for all eight numerical simulations as a function of distance, depicting the effects of wavefield scattering on ground-motions in the regime $k_w.a << 1$. Panels (a) and (b) depict MPR for media with H=0.1 and H=0.5, respectively. Grey dashed lines are plotted to facilitate the MPR comparison in two nearby panels. Wavefield scattering is proportional to correlation length, Hurst

exponent, and the standard deviation of medium heterogeneities. The highest values of $k_w.a$ for correlation lengths of 5 and 10 km are 0.27 and 0.54, respectively.

List of Tables

Table 1: Parameters for the 28 computational 3D Earth models generated for this study.

Model Reference	Correlation length *a* (km)	Standard deviation *σ* (%)	Hurst exponent *H*
M1, M1-L	1.0	5	0.1
M2, M2-L, M2-EL	5.0	5	0.1
M3, M3-EL	10.0	5	0.1
M4, M4-L	1.0	10	0.1
M5, M5-L, M5-EL	5.0	10	0.1
M6, M6-EL	10.0	10	0.1
M7, M7-L	1.0	5	0.5
M8, M8-L, M8-EL	5.0	5	0.5
M9, M9-EL	10.0	5	0.5
M10, M10-L	1.0	10	0.5
M11, M11-L, M11-EL	5.0	10	0.5
M12, M12-EL	10.0	10	0.5

Parameters of 28 computational 3D models generated using random fields characterized by von Karman autocorrelation functions (parametrized by correlation length, standard deviation and Hurst exponent). The suffixes "-L" and "-EL" indicate large and extra-large models, respectively.

List of Figures

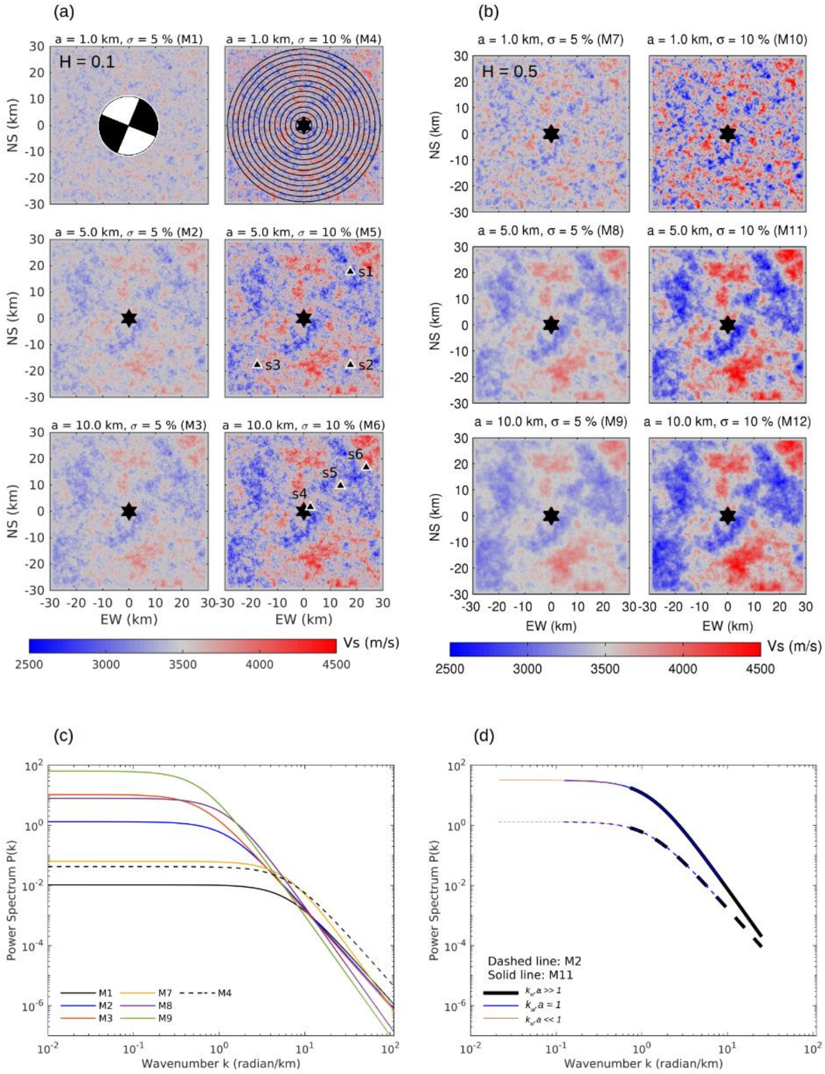

Figure 1: (a,b): S-wave speed distribution at the free surface for twelve 3D computational models for the regime $k_w.a \gg 1$, generated using three correlation lengths (1.0 km, 5.0 km, 10.0 km), two standard deviations (5%, 10%) and two Hurst exponents (0.1, 0.5). The black star marks the epicenter. The sites used for waveform comparison (black triangles, s1, s2, s3, s4, s5 and s6) and ground-motion analysis (black dots in circular rings) are also shown. The beach ball shows the focal mechanism of the earthquake source. Panels (a) and (b) depict random media with Hurst exponent 0.1 and 0.5, respectively. **(c):** Theoretical 1-D power spectra (PSD) for 3D Earth structure for seven selected models. Correlation length and Hurst exponent alter the shape of the power spectra (solid lines), whereas standard deviation only scales the PSD (mark dashed line; notice the scaling of M4 compared to M1, but their identical shape). **(d):** The theoretical power spectra of the random media are constrained by the dimensions of the computational model and the spatial grid size. The dashed and solid lines are spectra related to models M2 and M11, whereas three different colors depict power spectra sampled according to the three scattering regimes.

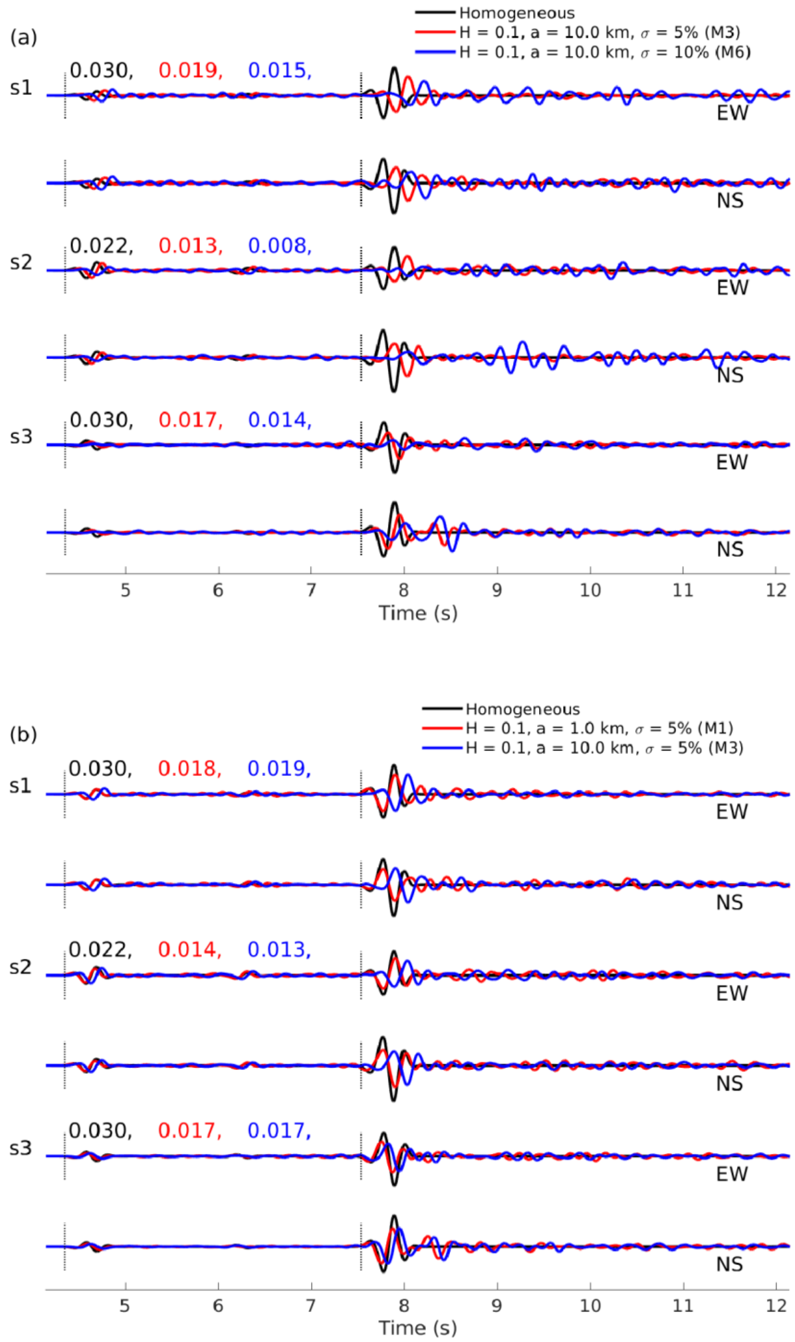

Figure 2: Horizontal components (East-West, EW, and North-South, NS) of ground acceleration (m/s^2) at sites s1, s2, s3 (Fig 1a). Black dotted lines indicate theoretical P- and S-wave arrival times in the considered homogeneous medium. Color-coded numbers indicate PGA values at individual sites. Waveforms are normalized by their PGA-value in the homogeneous-medium simulations for a given site. (a) Illustration of scattering controlled by σ for $k_w.a \gg 1$ and small H; (b) Illustration of negligible effects of correlation length on scattering for $k_w.a \gg 1$ and small H.

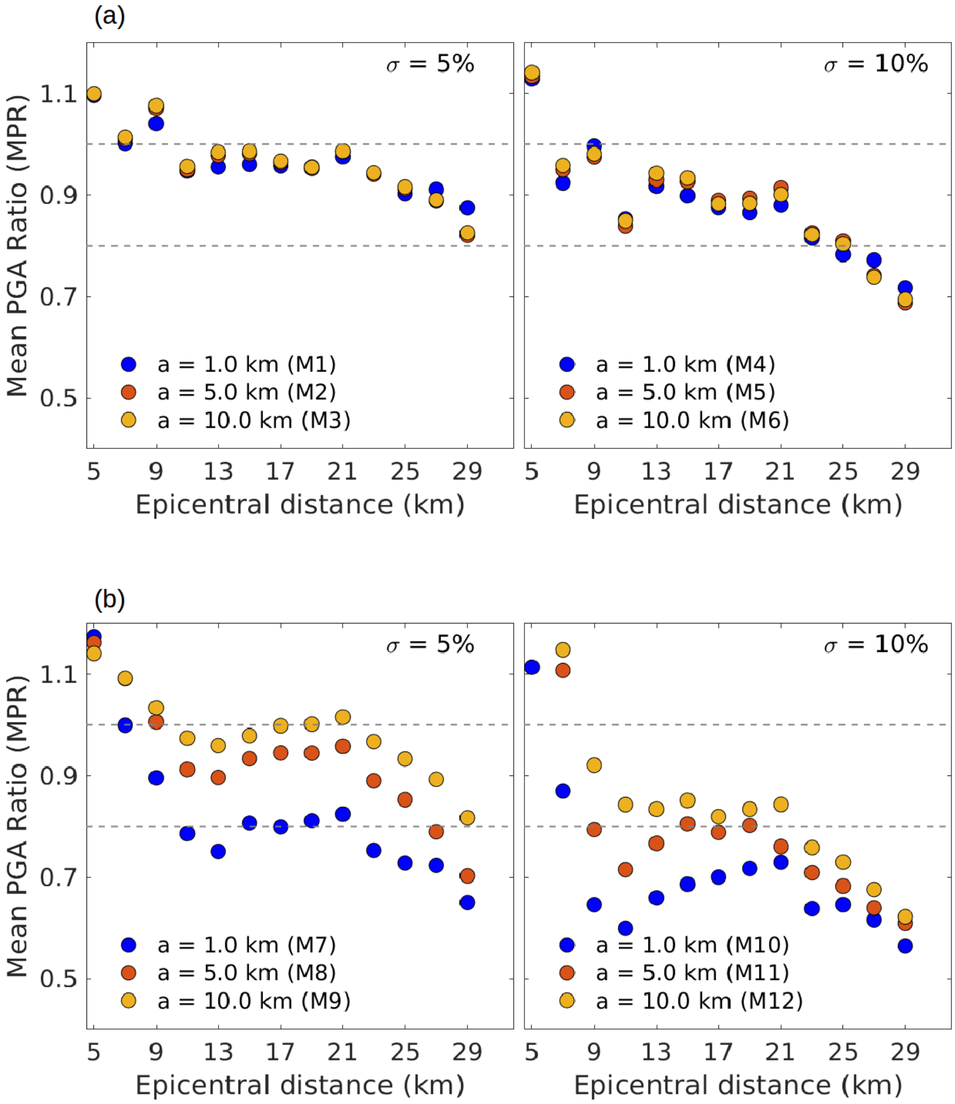

Figure 3: Mean PGA ratios (MPR) for all twelve numerical simulations as a function of distance, depicting the effects of wavefield scattering on ground-motions in the regime $k_w.a \gg 1$. Panels (a) and (b) depict MPR for media with H=0.1 and H=0.5, respectively. Grey dashed lines are plotted to facilitate the MPR comparison in two nearby panels. Wavefield scattering is proportional to the standard deviation of medium heterogeneities, and inversely proportional to correlation length for large Hurst exponent (H= 0.5), but remains nearly unaffected by variations in correlation length for small Hurst exponent (H= 0.1). The $k_w.a$ maxima for correlation lengths of 1, 5 and 10 km are 9.07, 45.36 and 90.72, respectively.

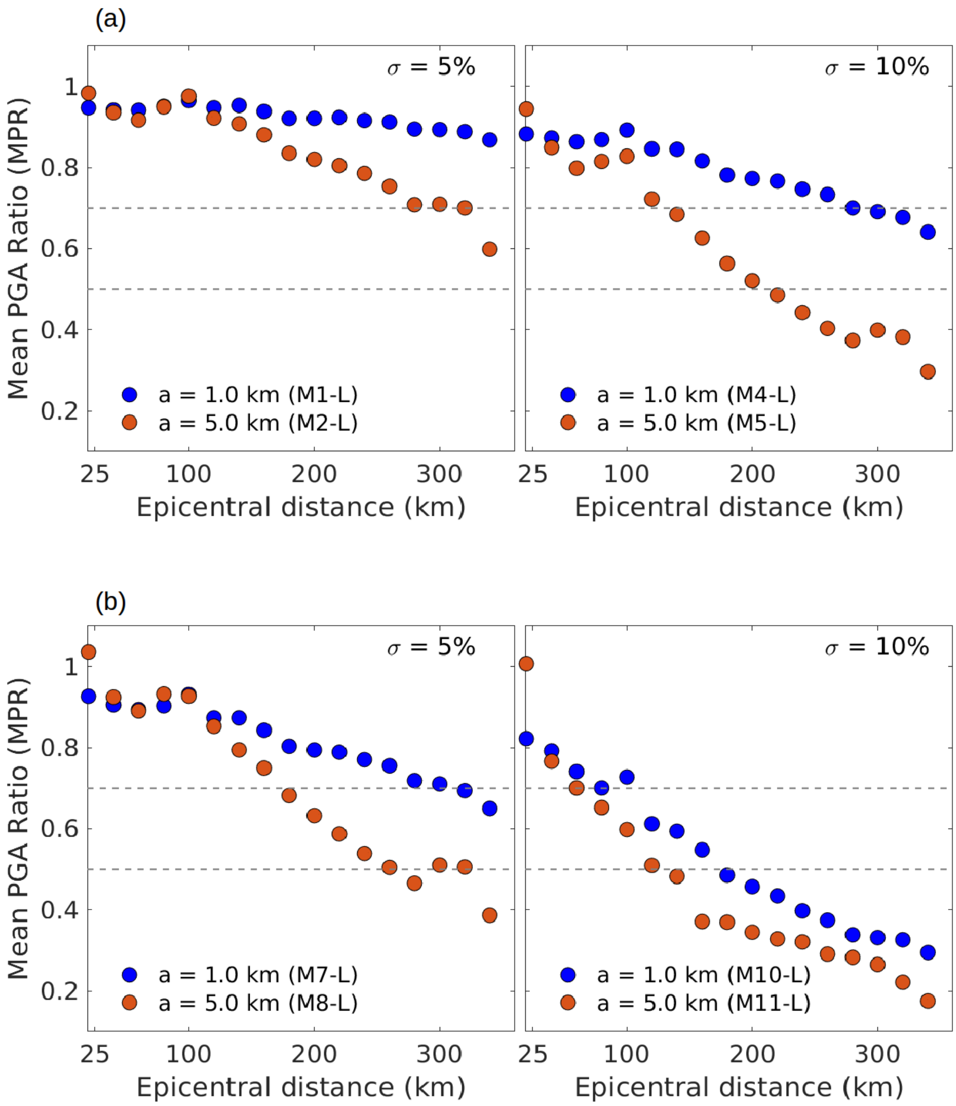

Figure 4: Mean PGA ratios (MPR) for eight numerical simulations as a function of distance, depicting the effects of wavefield scattering on ground-motions in the regime $k_w.a \approx 1$. Panels (a) and (b) depict MPR for media with H=0.1 and H=0.5, respectively. Grey dashed lines are plotted to facilitate the MPR comparison in two nearby panels. Wavefield scattering is proportional to correlation length, Hurst exponent, and standard deviation of medium heterogeneities. The highest values of $k_w.a$ for correlation lengths of 1 and 5 km are 0.90 and 4.53, respectively.

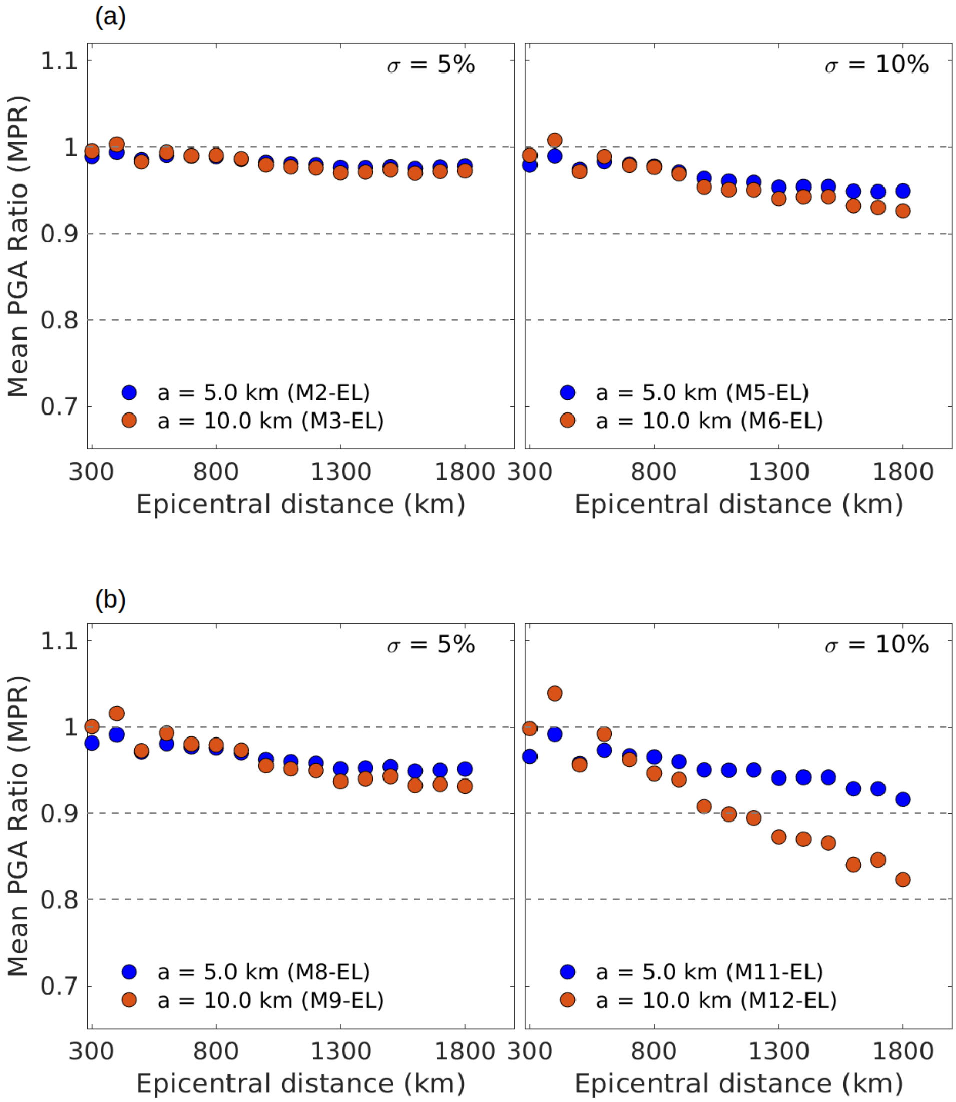

Figure 5: Mean PGA ratios (MPR) for all eight numerical simulations as a function of distance, depicting the effects of wavefield scattering on ground-motions in the regime $k_w.a << 1$. Panels (a) and (b) depict MPR for media with H=0.1 and H=0.5, respectively. Grey dashed lines are plotted to facilitate the MPR comparison in two nearby panels. Wavefield scattering is proportional to correlation length, Hurst exponent, and the standard deviation of medium heterogeneities. The highest values of $k_w.a$ for correlation lengths of 5 and 10 km are 0.27 and 0.54, respectively.